Physics of Fluids

Turbulent flow characteristics around a non-submerged rectangular obstacle on the side of an open channel

Cite as: Phys. Fluids **33**, 045106 (2021); https://doi.org/10.1063/5.0042914
Submitted: 05 January 2021 • Accepted: 16 March 2021 • Published Online: 02 April 2021

SeokKoo Kang, Ali Khosronejad and Xiaolei Yang

Physics of Fluids ARTICLE scitation.org/journal/phf

Turbulent flow characteristics around a non-submerged rectangular obstacle on the side of an open channel

Cite as: Phys. Fluids 33, 045106 (2021); doi: 10.1063/5.0042914
Submitted: 5 January 2021 · Accepted: 16 March 2021 ·
Published Online: 2 April 2021

SeokKoo Kang,[1,a)] Ali Khosronejad,[2] and Xiaolei Yang[3]

AFFILIATIONS

[1]Department of Civil and Environmental Engineering, Hanyang University, Seoul, South Korea
[2]Department of Civil Engineering, Stony Brook University, Stony Brook, New York 11794, USA
[3]State Key Laboratory of Nonlinear Mechanics, Institute of Mechanics, Chinese Academy of Sciences, Beijing 100190, China

[a)]Author to whom correspondence should be addressed: kangsk78@hanyang.ac.kr

ABSTRACT

The three-dimensional flow structure and turbulence characteristics around a non-submerged rectangular obstacle in an open channel are explored using numerical simulation. In particular, a low length-to-depth ratio condition, shown to be associated with three-dimensional flow features in our previous study, is considered. To sufficiently resolve all the important details of the three-dimensional turbulent flow around and in the entire wake of an obstacle, high-resolution large-eddy simulation (LES) employing is carried out on a parallel supercomputer. The LES results were compared with the measurements and analyzed to examine the horseshoe vortex structure, free-surface vortex structure, recirculation zones, vortex shedding process, turbulence characteristics, and wall shear stress distribution around an obstacle. The results provide important insights into the complete three-dimensional flow structure and wall shear stress patterns around the obstacle.

I. INTRODUCTION

Flow mechanisms around obstacles in rivers or streams have been an important research area in the water resources community. Examples of these obstacles are boulders, rock piles, tree trunks, logs, and concrete blocks. Such man-made or natural obstacles in a channel, known as instream structures, have been widely used for the management and restoration of small streams as well as large rivers such as the Yellow River in China; Mississippi and Sacramento Rivers in North America; and the Danube and Vistula Rivers in Europe.[1,2] Instream structures have been widely used for scour protection, bank stabilization, and aquatic habitat rehabilitation by modifying the flow and sediment transport processes in a channel.

One of the simplest (but the most studied) types of instream structure is a rectangular obstacle installed with its one end and is attached to a bank of the channel. This is also known as a spur dike or groin. These structures can be designed to be either submerged or non-submerged under specific flow conditions. Submerged and non-submerged obstacles refer to obstacles with water level above and below their crest, respectively. A major difference between a classical rectangular bluff body that has been studied in the fluid mechanics community[3,4] and a rectangular obstacle installed in an open channel is that the latter has additional boundaries, which are the free surface, sidewalls, and the channel bed. These additional boundaries introduce additional dimensionless parameters other than the Reynolds number, including the Froude number, length-to-depth ratio, width-to-depth ratio, and submergence ratio. It is well documented in the literature that the flow around a two-dimensional bluff body, such as a circular or rectangular cylinder, is characterized by von Kármán-type vortex shedding and flow separation in the wake. At moderate to high Reynolds numbers, the flow in the wake is known to become fully turbulent. The flow characteristics of obstacles in an open channel with various dimensionless parameters have not been well documented. Of the aforementioned dimensionless parameters, the most important, especially for non-submerged obstacles, may be the length-to-depth ratio. According to Chen and Jirka,[5] the three-dimensionality and complexity of the wake of a non-submerged obstacle in an open channel are determined by the wake stability parameter $S = c_f L/H$, where cf is the bottom friction parameter, L is the characteristic length of a body, and H is the depth. They observed that the wake tends to become shallow with increasing S, indicating that the flow enters a

two-dimensional and quasi steady state, in which the von Kármán-type vortex shedding is suppressed. If we limit our interest to cases under laboratory conditions, where *cf* has an approximately constant value of 0.01,[6] the only remaining parameter is the length-to-depth ratio, L/H.

Of particular interest in this study is the flow field around a non-submerged rectangular obstacle with a low length-to-depth ratio. One of the main difficulties in studying flow past such an obstacle, either experimentally or numerically, is associated with the fact that the wake size is very large. Consequently, the investigation of a three-dimensional and turbulent velocity field for the entire wake of the obstacle at a resolution fine enough to identify important flow features would be costly and time consuming. Presumably, this is why, in several previous studies that investigated instream structures at a low length-to-depth ratio, the velocities were measured or analyzed mostly in the vicinity of the obstacles.[7–9] Further, there are only a handful of studies that have attempted to measure the velocity and turbulent stress fields for the entire wake of a non-submerged obstacle with low[10] and high[11] L/H conditions at a resolution fine enough to identify large-scale flow features throughout the wake.

The present study is motivated by a lack of reporting on the complete structure of the three-dimensional flow field and turbulence patterns in the entire wake of an obstacle with a low length-to-depth ratio. In particular, this study considers the experimental case studied by Jeon *et al.*,[10] in which the mean velocity and turbulent stress fields were measured using acoustic Doppler velocimetry (ADV) for a sidewall-attached rectangular obstacle with $L/H = 1.4$. To the best of our knowledge, this is the first study to report detailed three-dimensional velocity measurements for a domain large enough to contain the entire recirculation zone downstream of a non-submerged obstacle with a low L/H value. The velocities were measured at more than 5000 measurement points for up to 10 min at each location at two different flow rates. This measurement demonstrates that the flow both upstream and downstream of the obstacle is highly three-dimensional, unlike in the cases with higher L/H[11,12] where the vertical velocity in the wake region was observed to be nearly zero. Jeon *et al.*[10] discovered that the wake near the mid-depth horizontal plane is characterized by a large recirculation zone with its axis of rotation parallel to the vertical axis. Conversely, near the bed, the wake consists of two different flow structures, a horizontal recirculation zone with the same axis of rotation as that near the mid-depth, and another recirculating flow region near the downstream corner between the structure and bed with its rotational axis perpendicular to the flume sidewalls. Using flow visualizations and water surface measurements, a vortex system was discovered beneath the free surface in front of the obstacle, which rotated counter to the horseshoe vortex system at the lower front of the structure. Although Jeon *et al.*[10] discovered several important flow features around a non-submerged obstacle taking the velocity measurements at thousands of locations, much remains unknown about the complete structure of the flow field. In that study, the velocity data in the vicinity of the walls and the upper third of the depth could not be measured at all because of the inherent limitations of ADV for obtaining velocity data near the free surface and solid walls. Further, even the thousands of measurement points with a maximum spacing of 0.25 m ($0.83L$) insufficiently captured small-scale flow features. Moreover, it was impossible to investigate the spatial evolution of the instantaneous flow field (e.g., vortex shedding) using the ADV measurements.

This study aims to investigate the flow around the same obstacle that was studied by Jeon *et al.*[10] using large-eddy simulation (LES) to elucidate the complete flow structure both in the vicinity and in the entire wake. Although computationally expensive, LES has successfully simulated complex turbulent flows in open channels.[13–17] Compared to the Reynolds-averaged Navier–Stokes (RANS) approach, LES simulates with better accuracy turbulent flows with massive flow separation and high turbulence anisotropy. For instance, Kang and Sotiropoulos[14] demonstrated that LES accurately captured the flow separation and turbulence-driven secondary flow in a meandering channel, whereas the RANS simulation on the same grid failed. In the literature, some studies have employed LES to investigate the flow around a rectangular obstacle with a low L/H value. For instance, Koken and Constantinescu[18] and Koken and Constantinescu[19] conducted LES for an obstacle of $L/H = 1.5$ on a fixed and mobile bed flume, respectively, using approximately 4×10^6 grid nodes. In the first study, the computed and measured two-dimensional velocity vectors were compared across the width of the channel at the free surface. In Koken and Constantinescu,[20] similar simulations were carried out for an obstacle with the same L/H using approximately 7×10^6 grid nodes without a quantitative comparison between the measurement and computation. The main focus of the above-mentioned studies was to identify the flow structure in the close to the obstacle or scour hole, which may be why those studies employed only a few million grid nodes that were mostly clustered near the obstacles. Unfortunately, these studies did not present quantitative comparisons between the measured and computed three-dimensional velocity components and the Reynolds stresses throughout the wake region, despite such comparisons being essential for validating the LES results.

For a comprehensive understanding of three-dimensional flow phenomena and turbulence characteristics, LES was carried out in this study for a rectangular obstacle using a computational domain sufficiently large to encompass the entire downstream recirculation zone with the grid spacing small enough to resolve the viscous sublayers of the near-wall regions. A total of 160×10^6 grid points were used for the simulation. To ensure the accuracy of the simulation, quantitative comparisons between the measured and computed first- and second-order turbulence statistics were made throughout the wake region. Using the LES-computed flow field, the time-averaged and instantaneous flow fields were examined in detail to investigate three-dimensional flow structures, secondary current patterns, and the associated turbulence characteristics. This allows us to elucidate the complete structure of the flow, both in the vicinity and in the entire wake of a non-submerged obstacle at low L/H, for the first time.

The remainder of this paper is organized as follows. In Sec. II, the flow problem is described and the details of the numerical simulations are presented. In Sec. III, the LES-computed results are compared with the measurements, and thereafter, the instantaneous and mean flow fields are examined to study the flow structures, turbulence characteristics, and wall shear stress distributions. In Sec. IV, the main findings are summarized.

II. DESCRIPTION OF FLOW PROBLEM AND COMPUTATIONAL DETAILS

In the experimental study by Jeon *et al.*,[10] two flume experiments were conducted with different flow rates at the same depth. Similar dimensionless velocity fields between the two were observed. In the

present study, numerical simulations were carried out for the case with a lower flow rate only. The key parameters of the experiments are summarized in Table I. Of the listed parameters, L/H is the one that determines the shallowness (or two-dimensionality) of the flow in the wake.[5,10]

The LES was carried out using the computational fluid dynamics model developed by Kang *et al.*,[13] which solves the spatially filtered Navier–Stokes equations and continuity equations formulated in generalized curvilinear coordinates and closed with the dynamic Smagorinsky model,[21] on parallel supercomputers. An important feature of the model in comparison with other existing flow models for open channel flow applications is its capability to handle arbitrary complex geometries and an efficient computer algorithm for solving the equations on highly stretched grids. The computational model employs the curvilinear immersed boundary (CURVIB) method[22] for handling a moving/stationary immersed boundary (channel bathymetry and/or instream structures) embedded in a background computational domain, that is, discretized with a boundary-fitted curvilinear mesh. The CURVIB method treats the immersed boundary as a sharp interface, and the boundary conditions are reconstructed at curvilinear grid nodes adjacent to the boundary using interpolation along the local normal to the boundary direction.[13] For the solution of the momentum equations and Poisson equation for pressure, a highly efficient Newton–Krylov method and an algebraic multigrid method are employed, respectively. The flow model has been successfully applied to numerous turbulent flow problems, including flow in meandering channels,[13,14,23,24] flow in large rivers,[25,26] flow around instream structures,[17,27–31] flow past hydrokinetic turbines,[32,33] flow in a wind farm,[34] flow through coastal drainage gates,[35] a flash flood event,[36] and sediment transport processes.[37–40] Details about the governing equations and numerical methods are omitted for the sake of brevity, but they can be found in Refs. 13 and 41.

LESs were carried out on two grids—Grid I and II—with different grid resolutions to check the grid convergence of the computed result. As the LES on Grid I was run as a benchmark case, a smaller domain size was used compared to the LES on Grid II. Table II provides details of the computational setup, including the grid information. Grids I and II, respectively, consist of approximately 57 and 162 $\times 10^6$ grid nodes. The minimum and maximum grid spacing of Grid I were 3 and 266 wall units, respectively, and those of Grid II were 0.8 and 70 wall units. The coordinates, computational domains, and grids together with the embedded obstacle (immersed boundary) are shown in Fig. 1. The x, y, and z directions indicate the streamwise, spanwise, and vertical directions, respectively. The locations of the domain outlets were determined not to interfere with the recirculation region, the size of which was approximately $12L - 13L$ in the experiment.[10]

TABLE I. Flow and geometrical parameters. g denotes the acceleration due to gravity. u_τ was determined by fitting the log-law to the vertical profile of the streamwise velocity measured[10] upstream of the obstacle.

Parameters	Values
Flow depth at the tailgate (H)	0.215 m
Flume width (B)	0.9 m
Streamwise dimension of the obstacle (t)	0.04 m
Cross stream dimension of the obstacle (L)	0.3 m
Length-to-depth ratio (L/H)	1.4
Volume flow rate (Q)	2.78×10^{-2} m^3/s
Mean velocity (U_0)	0.144 m/s
Froude number ($Fr = U_0/\sqrt{gH}$)	0.10
Kinematic viscosity (ν)	1.03×10^{-6} m^2/s
Reynolds number ($Re = U_0H/\nu$)	3.00×10^4
Friction velocity (u_τ)	0.007 m/s

TABLE II. Details of the computational setup. The superscript $^+$ denotes the viscous length and time scales made dimensionless using ν and u_τ. $l^+ = u_\tau l/\nu$ (l is x, y, or z) and $t^+ = u_\tau^2 t/\nu$. Δ denotes grid spacing.

Computational details	Grid I	Grid II
Streamwise domain extent	$-3.33 \le x/L \le 16.67$	$-6 \le x/L \le 23.33$
$N_x \times N_y \times N_z$	$811 \times 483 \times 146$	$1354 \times 541 \times 221$
Total number of nodes	5.71×10^7	1.62×10^8
Δx	2.5–38 mm	2–10 mm
Δx^+	18–266	14–70
Δy	0.4–2.5 mm	0.12–2.0 mm
Δy^+	3–18	0.8–14
Δz	0.4–2.5 mm	0.12–2.5 mm
Δz^+	3–18	0.8–18
Δt	3×10^{-3} s	2.5×10^{-3} s
$\Delta t^+ (= u_\tau^2 \Delta t/\nu)$	0.15	0.12
$\Delta t^* (= U_0 \Delta t/L)$	1.44×10^{-3}	1.20×10^{-3}

The maximum measured free-surface elevation difference throughout the experimental flume[10] was approximately 2 mm or 1% of the mean depth. This means that the free surface can be assumed to be a flat plane with zero shear stress. In the computation, the rigid-lid approximation[42] that treats the free surface as a frictionless plane surface was employed. Thus, the top boundary ($z = H$) was treated as a shear-free plane surface, at which no-flux and free-slip boundary conditions were imposed for instantaneous velocities. At the inlet plane, instantaneous turbulent velocity fields, which were saved from a separate LES solving the fully developed turbulent flow with streamwise periodicity, were fed to reproduce the fully developed turbulent incoming flow condition. At the outlet plane, the zero-gradient condition was enforced for instantaneous velocities. At the bed ($z = 0$) and sidewalls ($y/L = 0$ and 3), the no-slip velocity condition was imposed for the LES on Grid II because the minimum near-wall grid spacing was approximately 1. For the LES on Grid I, however, the near-wall model of Wang and Moin[43] was employed because the near-wall region is not fully resolved in this case. Nevertheless, it is shown in Sec. III that the influence of the different near-wall resolutions and boundary conditions on the computed result is negligible. At the immersed boundary nodes, a near-wall model that imposes a shear stress boundary condition proposed by Kang[44] was employed. Wall models for immersed boundary methods are typically implemented by imposing a velocity boundary condition at the first off-wall immersed boundary (IB) node, assuming the log-law distribution of the velocity. Such a method, which imposes only a velocity condition, can yield inaccurate wall shear stress unless a sufficiently fine grid resolution is

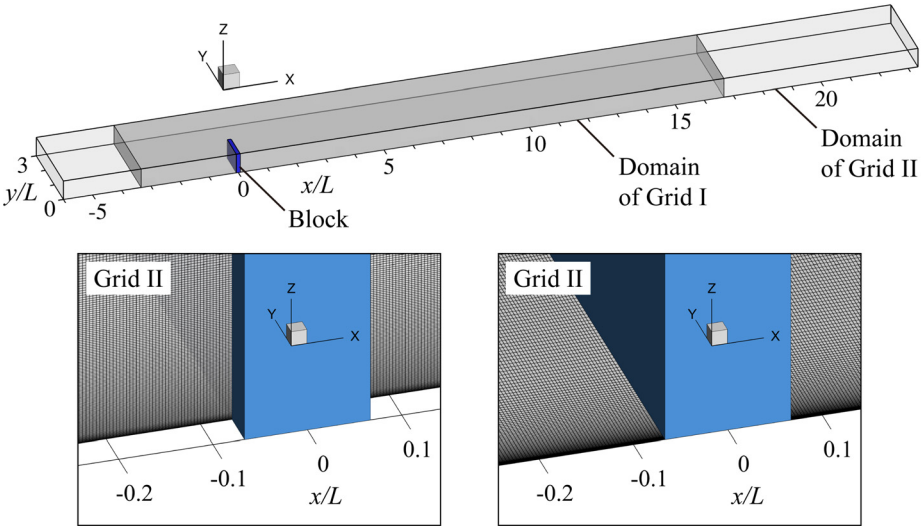

FIG. 1. The coordinate system, computational domain, and grid.

employed. Kang[44] proposed a novel method that imposes a shear stress boundary condition together with a velocity condition at the IB node by modifying the subgrid scale–eddy viscosity at the IB node.

The LESs were first run until the total instantaneous kinetic energy of the computational domain reached a steady state that took about 2×10^5 time steps. Subsequently, the instantaneous flow field in the domain was averaged for 10^6 time steps on Grid I and for 4×10^5 time steps on Grid II. The total physical sampling times on Grids I and II were 50 and 16 min, respectively. For the same obstacle considered herein, Jeon *et al.*[10] showed experimentally that the sampling of the velocities for 10 min was sufficient for obtaining converged statistics even at a location in the downstream recirculation zone. The integral time scales measured in the flume were approximately between 0.5 and 2 s,[10] which means that the 10, 16, and 50-min sampling times correspond to at least 300, 480, and 1500 integral time scales, respectively. The LESs were run on 400 cores of a Linux cluster supercomputer comprised of Intel Xeon E5–2650 v3 2.3 GHz central processing units (CPUs) interconnected by FDR (fourteen data rate; 56 Gb/s) InfiniBand Mellanox adapters and a switch. To average the flow fields, the LESs were run continuously for approximately 40 and 75 days for Grids I and II, respectively, on the supercomputer.

III. LES RESULTS AND DISCUSSION

In this section, the computed LES results are presented. The LES-computed results are first compared with the experimental data[10] to demonstrate the accuracy of the simulation, and then, the computed flow fields are investigated to study the three-dimensional flow structures, turbulence characteristics, and wall shear stress patterns around the obstacle.

The variables and notations used in the remainder of this paper are defined as follows. u, v, and w are the instantaneous velocity components in the x, y, and z directions, respectively. $\langle\rangle$ is the mean (time-averaged) component of a flow variable, and the superscript $'$ denotes the temporally fluctuating component. k is the turbulence kinetic energy defined as $k = \frac{1}{2}(\langle u'u' \rangle + \langle v'v' \rangle + \langle w'w' \rangle)$.

A. Comparisons between the LES and measurement

Comparisons of the time-averaged velocities and Reynolds stresses are presented in Figs. 2 and 3. These figures compare the spanwise profiles of $\langle u \rangle / U_0$, $\langle v \rangle / U_0$, $\langle w \rangle / U_0$, k/U_0^2, $\langle u'v' \rangle / U_0^2$, and $\langle w'u' \rangle / U_0^2$ at various streamwise locations in the $z = 0.09H$ and $0.51H$ planes. As can be seen, both LESs show very good agreement with the measurements. Namely, all three velocity components and second-order turbulence quantities are predicted with high accuracy. The LES also produces a nearly grid-independent result in most locations. The above comparisons demonstrate that the LES result on Grid II is accurate with respect to the measurement and no further grid refinement is necessary.

B. Instantaneous vortical structures

In Fig. 4(a), the instantaneous vortical structures in the vicinity of the obstacle are visualized using the λ_2 criterion method proposed by Jeong and Hussain,[45] a reliable vortex identification method widely used in the fluid mechanics community. The figure reveals two horizontally oriented arch-like elongated vortex structures before the obstacle, one near the bed and the other near the free surface. The one near the bed is associated with the formation of a horseshoe vortex system before the obstacle that also has been reported in other studies.[10,18] The one near the free surface indicates a vortical structure beneath the free surface, the existence of which was discovered by Jeon *et al.*[10] They observed a reversed flow region at the free surface before the obstacle using a flow visualization technique, which suggested the presence of a vortex system directing the flow at the free surface away from the obstacle. This vortex is hereafter referred to as the free-surface vortex. Figure 4(a) also shows a series of vertically oriented vortical structures that start from the upstream edge of the obstacle. These structures are associated with vortex shedding from the edge, which forms a shear layer between the regions inside and outside the wake of the obstacle.

To compare the vortical structures at different elevations, the isosurfaces of constant λ_2 are plotted for three different zones, $z/H < 0.4$ (bottom), $0.4 < z/H < 0.8$ (middle), and $z/H > 0.8$, and viewed

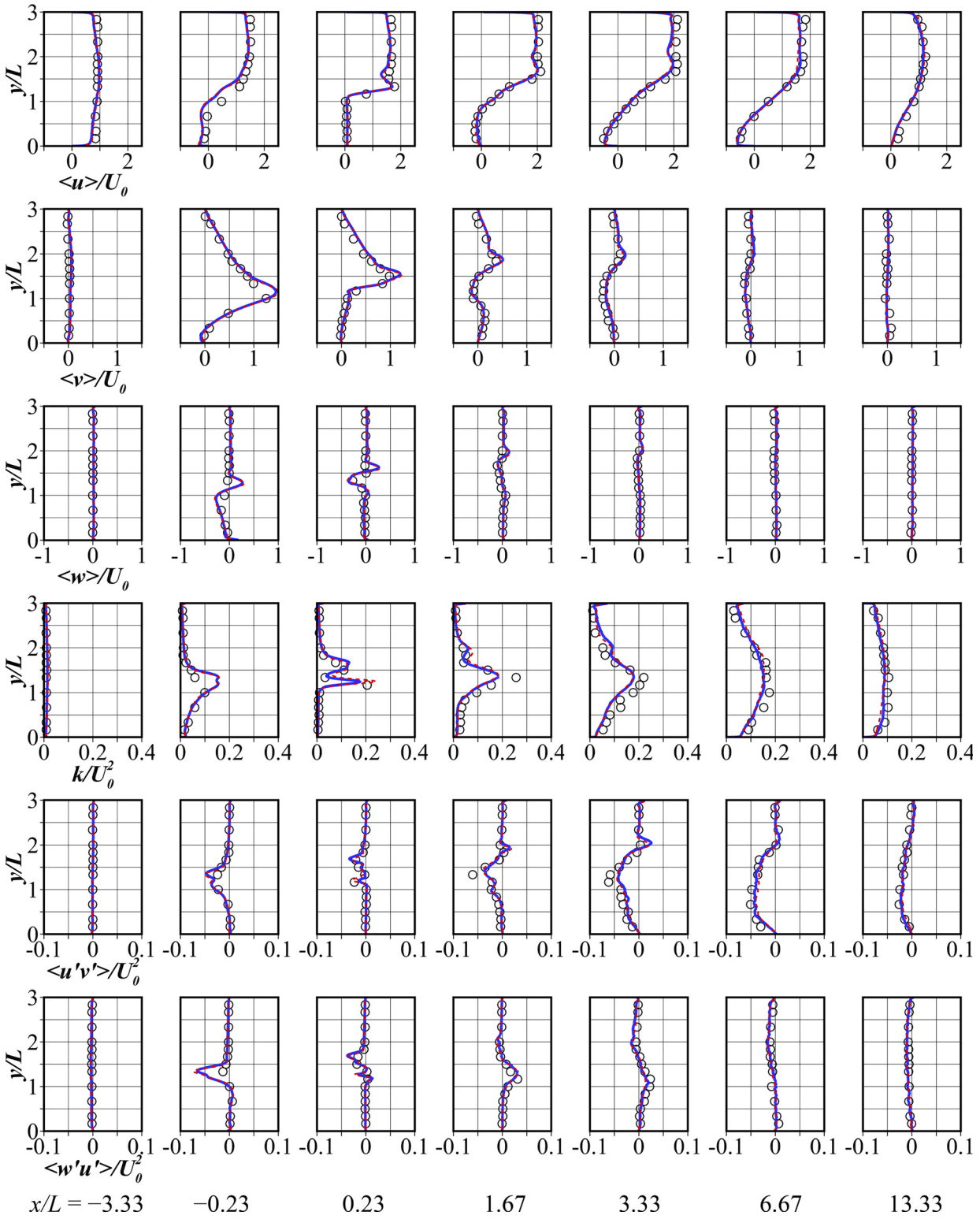

FIG. 2. Comparisons of the spanwise profiles of the computed (lines) and measured (symbols) mean three-dimensional velocities (u, v, and w), turbulence kinetic energy (k), and $\langle u'v' \rangle$ and $\langle w'u' \rangle$ Reynolds stresses at various streamwise locations on the $z = 0.09H$ plane (Grid I: red dashed line, Grid II: blue solid line, circle: ADV measurement).

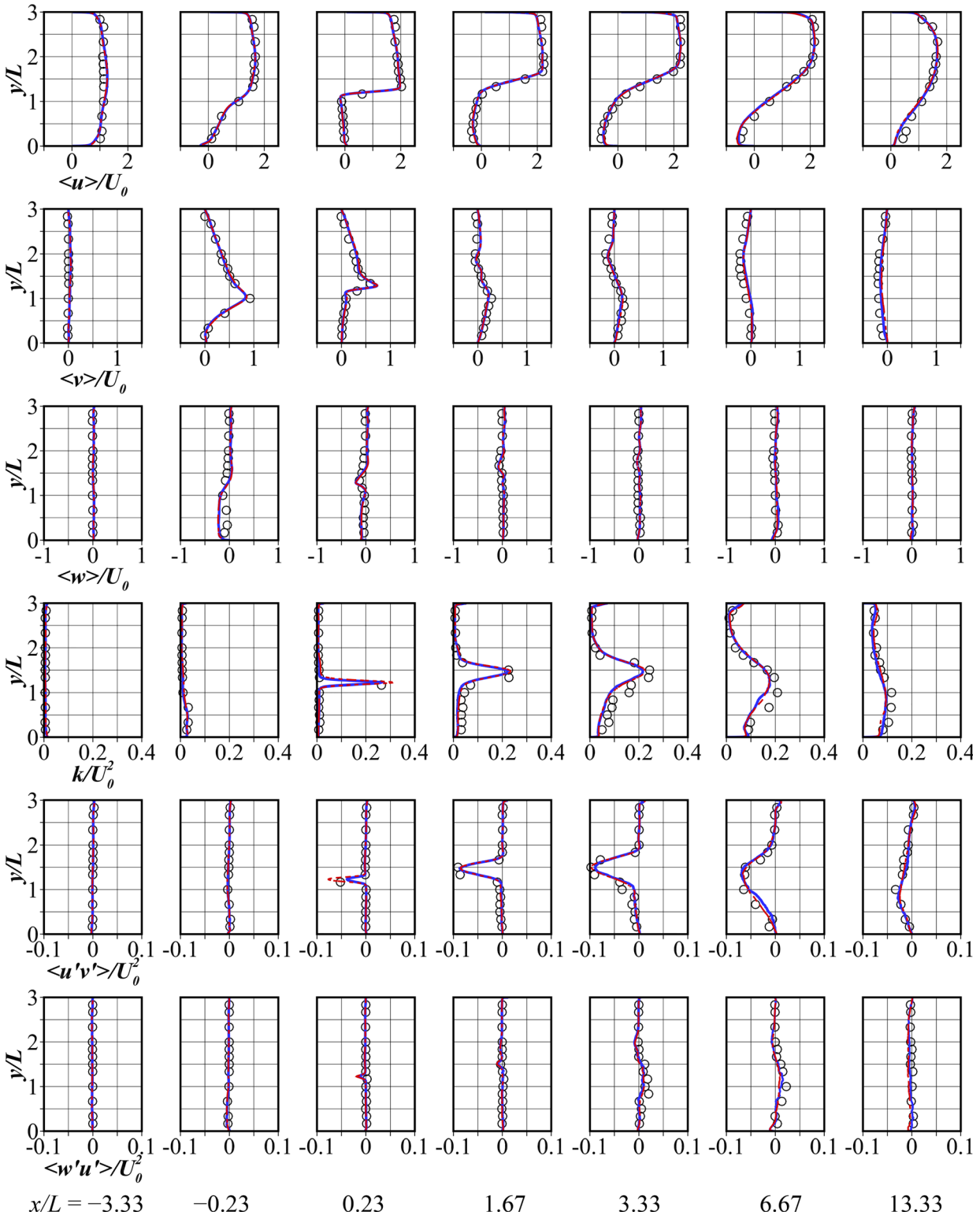

FIG. 3. Comparisons of the spanwise profiles of the computed (lines) and measured (symbols) mean three-dimensional velocities (u, v, and w), turbulence kinetic energy (k), and $\langle u'v' \rangle$ and $\langle w'u' \rangle$ Reynolds stresses at various streamwise locations on the $z = 0.51H$ plane (Grid I: red dashed line, Grid II: blue solid line, circle: ADV measurement).

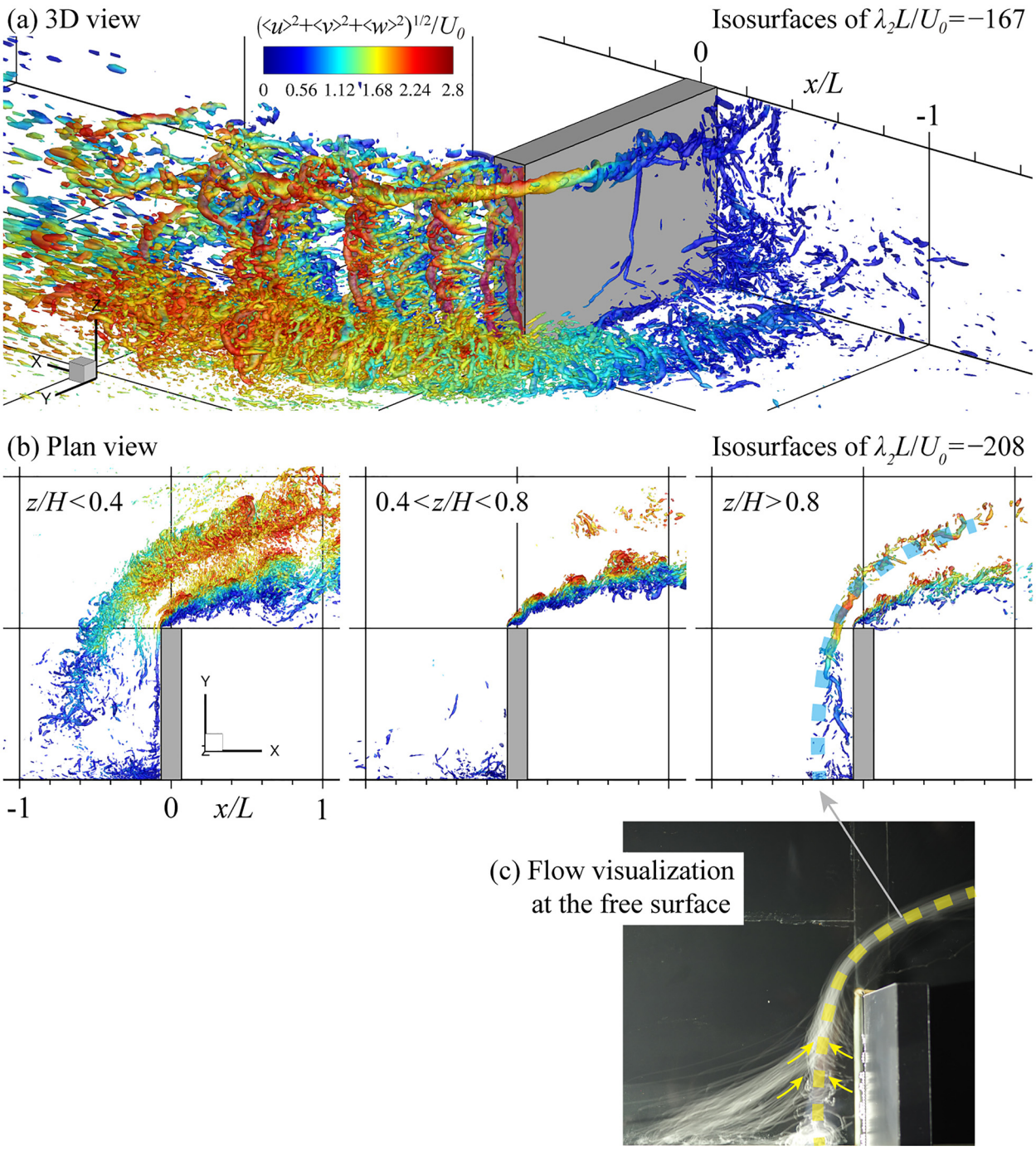

FIG. 4. LES-computed isosurfaces of (a) $\lambda_2 L/U_0 = -167$ and (b) –208 that are colored by the dimensionless velocity magnitude. (c) The flow visualization result at the free surface of the laboratory flume.

from a location above the obstacle in Fig. 4(b). In each zone, the isosurfaces outside the zone are removed for clarity. In the figure, vertically oriented shear layer vortices, which emanate from the upstream edge of the obstacle, are observed in all three regions, suggesting that the vortex shedding process is present throughout the depth. The vortices create similar arch-shaped trajectories regardless of their vertical locations. It is noticed that the shear layer vortices in the bottom region appear more dispersed in the spanwise direction compared to

those in the other regions, which is due to the higher turbulence intensities induced by the bottom friction. In the bottom and top regions, more arch-shaped structures are visible in addition to the shear layer vortices. Unlike the shear layer vortices, these vortical structures are detached from the obstacle. This indicates that those vortices are associated with reversed flow in front of the obstacle induced by the horseshoe and free-surface vortices. The flow visualization experiment by Jeon *et al.*[10] demonstrated the presence of a free-surface vortex before the obstacle. However, it could not be compared directly with the present LES results because of different image angles. In this study, to reconfirm the presence of a free-surface vortex and to compare the measured with computed vortical structure, another flow visualization experiment was performed in a laboratory flume. In that experiment, small floating Styrofoam particles were released upstream of the obstacle, and their motions were recorded at a location directly above the obstacle using an Olympus EM-5 Mark II camera with an exposure time of 6 s, which is equivalent to $2.88L/U_0$. The image is shown in Fig. 4(c). The white streaks in the image mark the trajectories of the particles recorded for 6 s. The particles form an arch-shaped trajectory to which the surrounding flows converge. The trajectory, which is marked by the dashed line in Fig. 4(c), is superimposed in Fig. 4(b), and as seen in the figure, its location shows very good agreement with that of the computed free-surface vortex. This corroborates the presence of the vortex system near the free surface originally discovered by Ref. 10 and demonstrates the accuracy of the present LES.

Coherent vortical structures in an instantaneous turbulent flow field can also be visualized by the locations of low pressure ($p' < 0$).[46] In Figs. 5 and 6, contours of the instantaneous pressure fluctuation p' together with the fluctuating velocity vectors (u', v', w') are plotted. In the figure, a negative value of p' (blue) that indicates a pressure below the mean pressure at a given location is associated with coherent vortices. Figure 5 shows the contours and vectors in three planes, $z/H = 0.1$, 0.5, and 1, and Fig. 6 shows those in the $y/L = 1.003$ plane. In Fig. 5, the fluctuating velocity vectors around the low-pressure zones (core of the shear layer vortices) show coherent rotational motions. The shear layer vortices remain coherent close to the upstream edge but lose coherence while moving downstream and merge with others to form a larger one. In Fig. 6, two circular regions of low pressure are identified near the free surface and bed that are the locations of the free-surface and horseshoe vortex systems. The close-up views reveal that the free-surface vortex rotates in the clockwise direction, whereas the horseshoe vortex rotates in the counterclockwise direction when viewed from the sidewall at $y/L = 3$. The above figures also show that the resolution of the LES is sufficiently fine to resolve the instantaneous vortical structures that are much narrower than the obstacle thickness.

To investigate the unsteadiness of the flow and vortex shedding processes around the obstacle, pressure fluctuation contours together with fluctuating velocity vectors are plotted at eight consecutive time steps in Figs. 7–9.

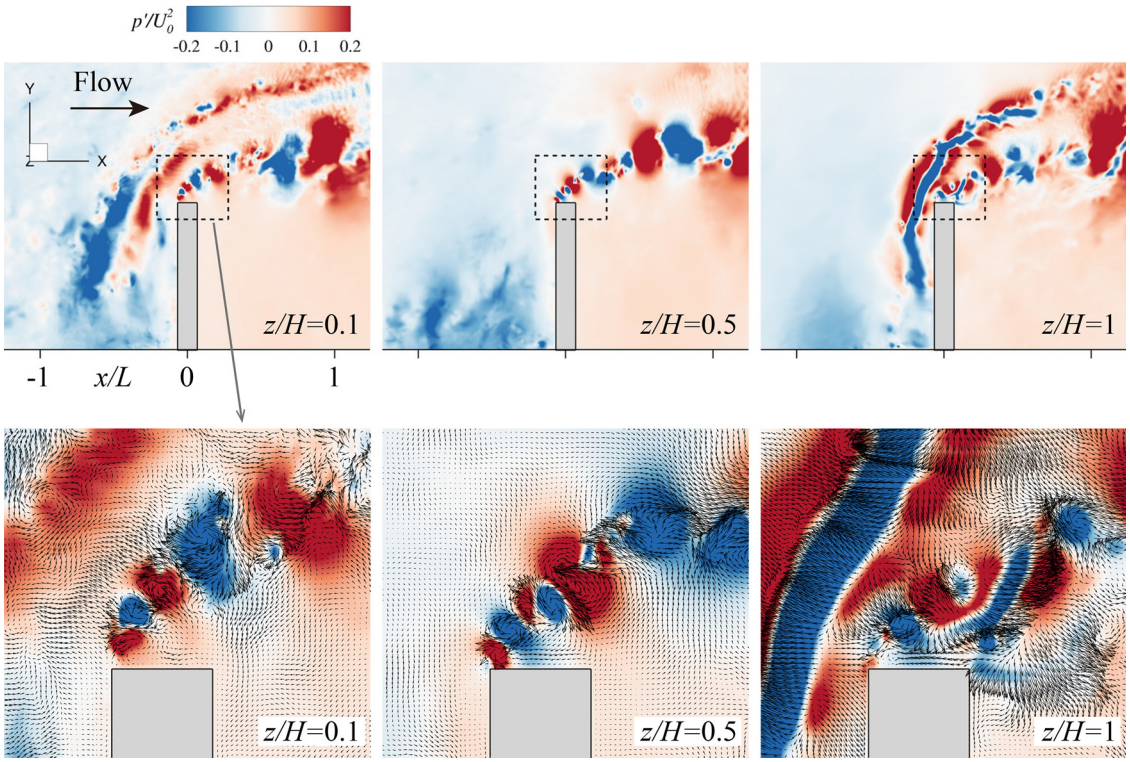

FIG. 5. Instantaneous pressure fluctuation (p') contours and fluctuating velocity vectors in the xy planes of $z/H = 0.1$, 0.5, and 1. The vectors are plotted on every second grid point in the x direction.

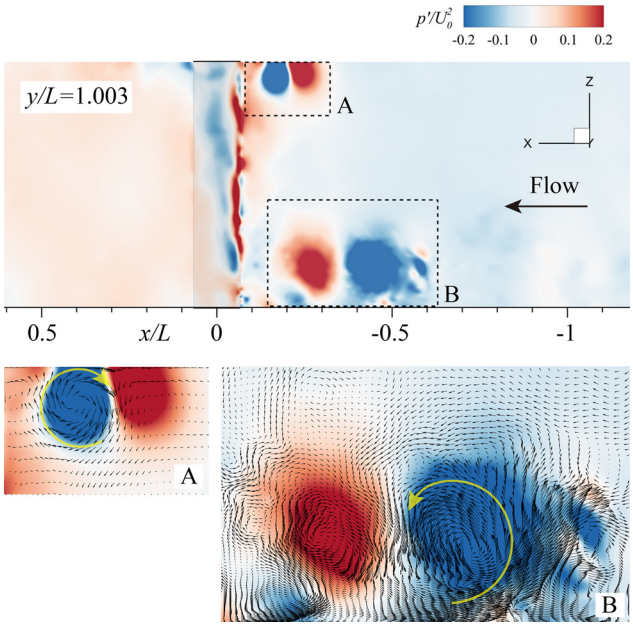

FIG. 6. Instantaneous pressure fluctuation (p') contours and fluctuating velocity vectors in the $y/L = 1.003$ plane. The vectors are plotted on every second grid point in the x and z directions.

Figures 7 and 8 show the instantaneous flow fields plotted on the $z/H = 0.5$ and 0.97 planes, respectively. The alternating low-pressure regions seen in Fig. 7 reveal well-defined vortices shedding from the tip of the obstacle. Compared to the $z/H = 0.5$ plane, the coherent motion of the vortices is not well-defined at the $z/H = 0.97$ plane. This is because the vertically oriented vortices near the free surface interfere with the free-surface vortex originating in front of the obstacle. An interesting feature that can be seen in Fig. 8 is that the shape and location of the free-surface vortex are not stationary. At $t = t_1$, the free-surface vortex is nearly attached to the upstream tip of the obstacle, but it moves back and forth over time. It can be seen that the thickness of the free-surface vortex changes continuously over time. The observations from Figs. 7 and 8 can be summarized as: (1) both near the free surface and at the mid-depth, there exists vertically oriented periodic vortex shedding from the upstream tip of the obstacle; (2) near the free surface, the vertically oriented vortices interact with the horizontally oriented free-surface vortex, which promote the breakdown of the vortex shedding; and (3) the position and shape of the free-surface vortex are not stationary but changes continuously over time.

In Fig. 9, the instantaneous flow fields are plotted on the $y/L = 0.67$ plane. At this plane, two distinct low-pressure zones are observed near the free surface and bed upstream of the obstacle, which are the footprints of the free-surface and horseshoe vortex systems. The non-stationary behavior of the free-surface vortex can be observed. Namely, the free-surface vortex moves away from the obstacle from $t = t_1$ to $t = t_4$, but it moves toward the obstacle from $t = t_5$ to $t = t_8$. The horseshoe vortex system near the bed also exhibits non-stationary behavior. From $t = t_1$ to $t = t_8$, the core of the horseshoe vortex moves toward the obstacle. During this time period, the size of the horseshoe vortex decreases considerably. It can be speculated that the horseshoe vortex possibly moves back and forth in the streamwise direction over time, like the free-surface vortex, at a certain frequency.

In Fig. 10, the velocity spectra at Points A, B, C, and D displayed in Figs. 7–9 are plotted to investigate the frequencies associated with the unsteadiness of the vertically oriented vortices, free-surface vortex, and horseshoe vortex.

First, the transverse velocity spectra at Points A and B show spectral peaks at $St = 4.48$ and 5.38, respectively, where $St = fL/U_0$ denotes the Strouhal number. In the laboratory experiment for the same obstacle, Jeon *et al.*[10] observed $St \approx 0.1$ in $x/L > 10$ and much higher Strouhal numbers $(0.5 - 2)$ in $0.83 \leq x/L \leq 5$. They observed that the peak Strouhal number decreases in the downstream direction in $x/L \leq 5$. They postulated that the low Strouhal number (0.1) in the far wake is associated with a large-scale wake instability, while higher Strouhal numbers in the near wake are induced by the instability of the shear layer separating from the obstacle. The peak Strouhal numbers observed at Points A and B are likely to be associated with the shear layer instability. The higher Strouhal numbers compared with the experiment (2 in Ref. 10 vs 4–5 in the LES) are because of the different sampling locations. Points A and B are much closer to the obstacle than the location $(x/L, y/L, z/H) = (0.83, 1.33, 0.51)$, where $St = 2$ was observed in the laboratory. Moreover, as Figs. 7 and 8 show, the streamwise vortex spacing increases in the streamwise direction, which explains the decrease in the peak Strouhal number in the streamwise direction in the experiment.[10]

Second, the streamwise velocity spectra at Points C and D reveal the peaks at $St \approx 0.04$ and 0.02, respectively. These frequencies are lower by an order of the magnitude than the frequency observed in the far wake of the obstacle (approximately 0.1)[10] and lower by two orders of magnitude compared to the shear layer frequency (4–5). Those frequencies demonstrate that the free-surface and horseshoe vortex systems in front of the obstacle (Figs. 7 and 8) oscillate periodically in time in the streamwise direction at very low frequencies.

C. Time-averaged streamlines

In this subsection, the time-averaged streamlines are analyzed to understand the three-dimensional flow structure around the obstacle.

The three-dimensional streamlines of the time-averaged flow are shown in Fig. 11. In Fig. 11(a), multiple recirculating flow regions (spiral streamlines) are evident. Both in the immediate upstream and downstream regions of the obstacle, spanwise oriented (rotating around the y axis) recirculating flows impinge on the walls. In addition, a vertically oriented (rotating around the z axis) recirculating flow zone is present downstream of the obstacle. This zone is hereafter referred to as the horizontal recirculation zone. Interestingly, the spatial extent of the horizontal recirculation zone varies with elevation. Specifically, the upper part of the recirculation zone is attached to the downstream face of the obstacle and is also connected to the spanwise oriented recirculating flow region downstream of the obstacle. Conversely, the lower part is located approximately L downstream of the obstacle. In short, the wake consists of multiple recirculating flow regions with different axes of rotation. This confirms that the flow in the wake of the obstacle is highly three-dimensional, unlike a non-submerged obstacle with high L/H, where the wake is approximately two-dimensional.[11]

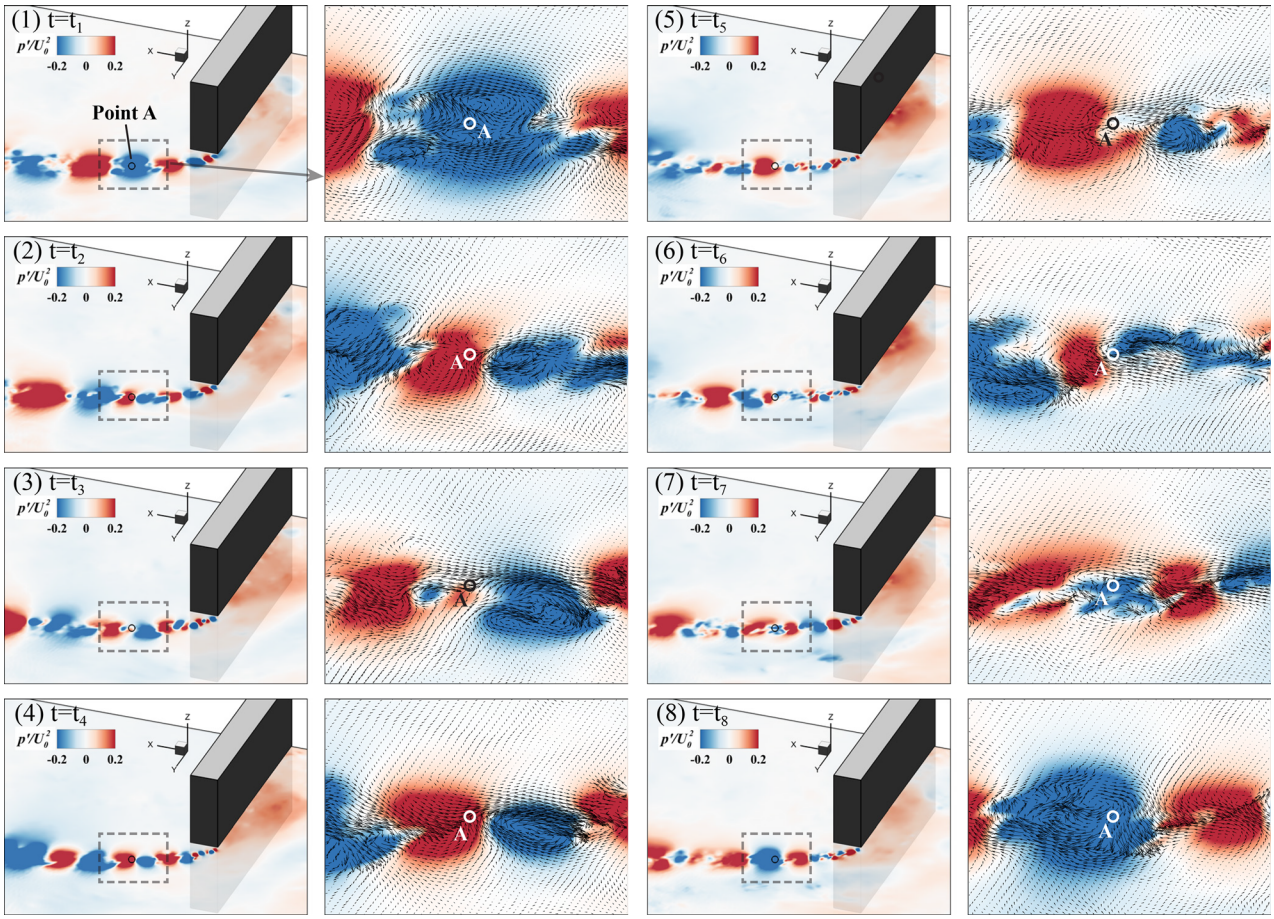

FIG. 7. Time evolution of pressure and velocity fluctuations at eight consecutive time steps displayed on the $z/H = 0.5$ plane. The vectors are plotted on every second grid point in the x direction. The time interval between each figure is $0.192L/U_0$. Velocity spectrum at Point A $(x/L, y/L, z/H) = (0.27, 1.23, 0.5)$ is shown in Fig. 10.

To visualize better the flow structures upstream of the obstacle, the streamlines in different parts of the upstream face are plotted in Figs. 11(b)–11(d). It can be seen that the streamlines of the incoming flow impinge on a point in the upstream face and spread radially in all directions over the surface. Figure 11(b) shows that part of the streamlines move toward the free surface to form spiral streamlines, or the mean free surface vortex. The streamlines then move horizontally toward the sidewall ($y = 0$) and center of the channel. Figure 11(c) shows the streamlines spreading toward the sidewall at $y = 0$ ultimately connecting to the spanwise oriented recirculation zone, or the mean horseshoe vortex. The mean horseshoe vortex system near the sidewall creates a large back flow region extending up to more than $1.5L$ from the obstacle. Owing to the presence of the horseshoe vortex region near the sidewall, the incoming streamlines near the bed are abruptly deflected toward the center of the channel. Figure 11(d) shows that the streamlines moving toward the center of the channel on the upstream face separate from the upstream edge. These streamlines are associated with the vertically oriented shear layer vortices observed in Fig. 4.

Figure 12 shows the time-averaged surface limiting streamlines displayed on the surfaces of the obstacle, the sidewall at $y = 0$, and the bed ($z = 0$). In the vicinity of the upstream face of the obstacle, reversed flow regions ($\langle u \rangle < 0$) are found, one at the bed and the other at the sidewall. As the two regions meet at the edge $(y, z) = (0, 0)$, it can be inferred that they comprise a single recirculation zone with a three-dimensional shape. This three-dimensional recirculation zone is associated with the horseshoe vortex system observed before the obstacle [Fig. 11(c)]. The streamline patterns on the sidewall show that the horseshoe vortex occupies the entire depth and extends up to $x/L \approx -2$ in the upstream direction. The horseshoe vortex is largest near the sidewall and becomes smaller as it moves toward the center of the channel. In the figure, two distinct lines can be found in the bed upstream of the obstacle and are labeled as Lines A and B. Line A originates from a separation saddle point S1 at the upstream end of the horseshoe vortex ($x/L \approx -2$). A saddle point is a singular point where two streamlines move inward and two others outward toward the point[47] and is associated with three-dimensional flow separation or attachment. Line B originates from another

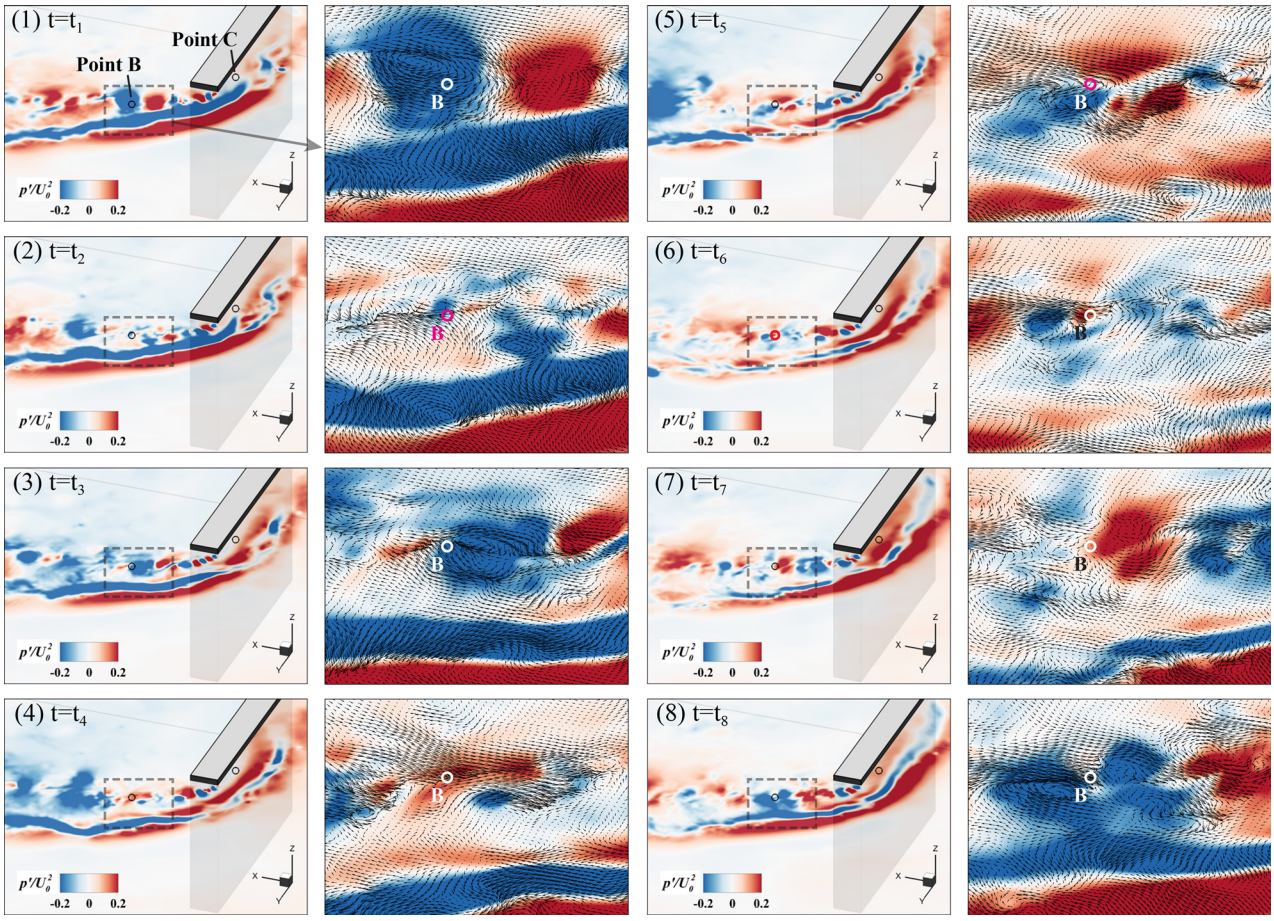

FIG. 8. Time evolution of pressure and velocity fluctuations at eight consecutive time steps displayed on the $z/H = 0.97$ plane. The vectors are plotted on every second grid point in the x direction. The time interval between each figure is $0.192L/U_0$. Velocity spectra at Points B $(x/L, y/L, z/H) = (0.27, 1.23, 0.97)$ and C $(-0.1, 0.83, 0.97)$ are shown in Fig. 10.

separation saddle point, S2, and develops along the boundary of the reversed flow region in the forward base of the obstacle. Streamlines similar to Lines A and B have been also observed around a surface-mounted rectangular block[48] and a wing body mounted on a flat surface,[49] both without a sidewall. According to Martinuzzi and Tropea,[48] Lines A and B, respectively, correspond to the upstream separation line and time-averaged location of the upstream boundary of the horseshoe vortex.

Between the lower edge of the upstream face of the obstacle and the recirculation zone formed by the horseshoe vortex, there is a narrow region with a positive $\langle u \rangle$. One can observe that Line C originates from the interface between that region and upstream recirculation zone and moves downstream, forming an arch-like trajectory. This indicates that vortex shedding occurs along Line C. The area between Lines B and C marks the lower part of the horseshoe vortex that rotates counterclockwise around the x axis in the downstream region $(x > 0)$. In the area between Lines C and D, the streamlines converge to Line D, which connects to the center of the downstream horizontal recirculation zone. The streamline directions in that area indicate that the entrainment of fluid occurs from the shear layer (Line C) toward Line D, which marks the boundary of the wake.

Another notable flow feature that can be observed in Fig. 12 is the downstream region that shows positive $\langle u \rangle$ immediately downstream of the obstacle. This region is associated with the spanwise oriented recirculating flow observed near the lower part of the downstream face of the obstacle in Figs. 11(a) and 12. Interestingly, two saddle points (S3 and S4) form around this region, in a similar way as S1 and S2 were formed around the horseshoe vortex. These streamline patterns and locations of the saddle points are very similar to those found in the upstream region and are nearly symmetric about $x = 0$.

The streamlines presented in Figs. 11 and 12 provide new insights into the three-dimensional flow structure around the obstacle, which can be summarized as follows. First, a horseshoe vortex system forms a three-dimensional shape recirculation zone upstream of the obstacle, the size of which is approximately $2L$ near the sidewall. The horseshoe vortex system leaves unique streamline patterns around the obstacle, namely Lines A and B. Second, below the free surface before

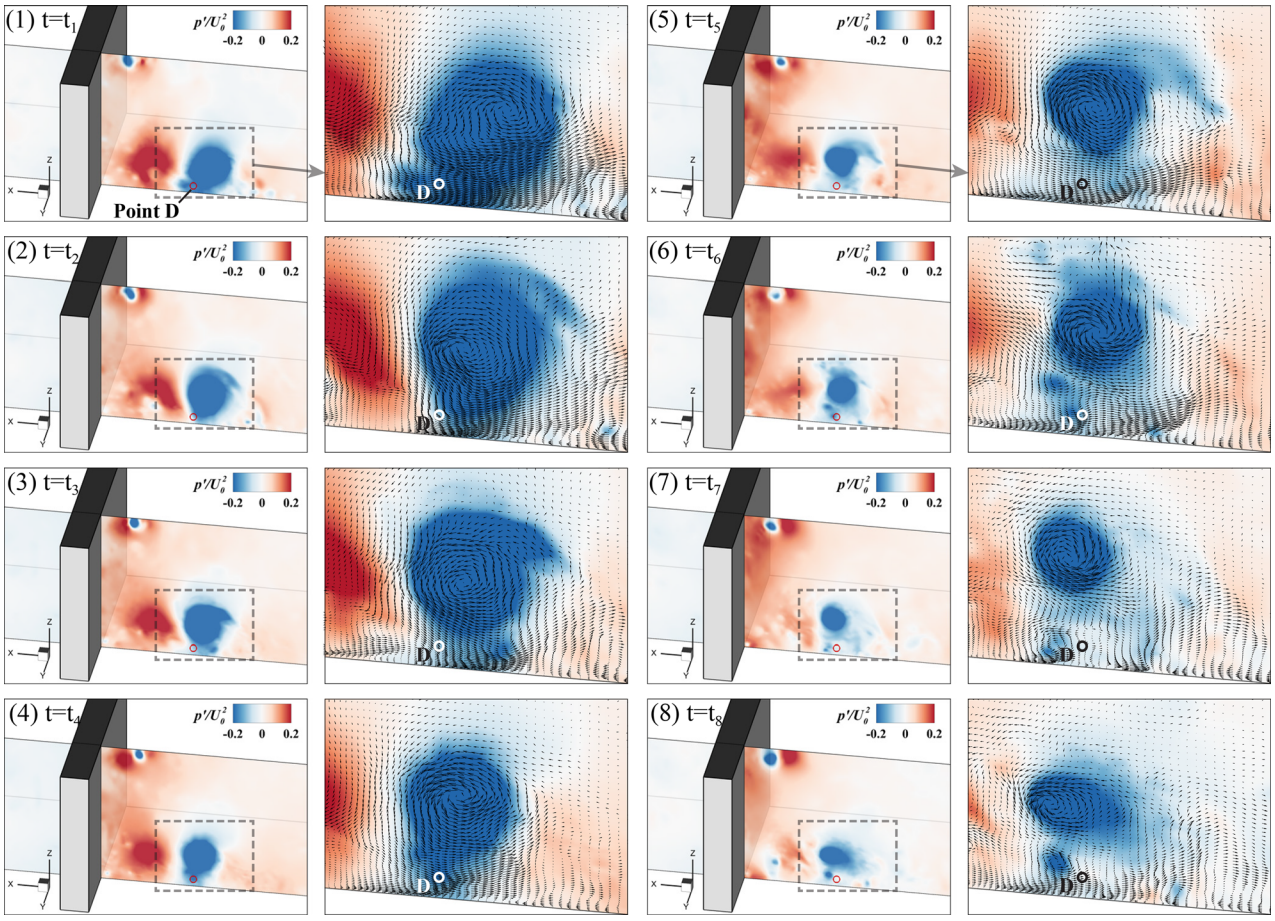

FIG. 9. Time evolution of pressure and velocity fluctuations at eight consecutive time steps displayed on the $y/L = 0.67$ plane. The vectors are plotted on every second grid point in the x direction, and every third grid point in the z direction. The time interval between each figure is $0.192L/U_0$. Velocity spectrum at Point D $(x/L, y/L, z/H) = (-0.5, 0.67, 0.05)$ is shown in Fig. 10.

the obstacle, a smaller vortex system that rotates counter to the horseshoe vortex is observed. Third, another horseshoe vortex-like flow pattern was found downstream of the obstacle. In our previous experimental study,[10] the detailed structure of the three-dimensional flow around the obstacle could not be examined because of insufficient spatial resolution (horizontal measurement spacing was $0.16L$–$0.33L$) and the inability of the ADV probe to measure the regions near the wall and free surface. These three-dimensional flow features were not observed for cases with high L/H and are likely to be associated with the low length-to-depth ratio ($L/H = 1.4$). For instance, Paik and Sotiropoulos[12] and Higham *et al.*[11] observed two-dimensional horizontal eddies attached to the downstream surface of the obstacles at $L/H = 26$ and 6.25, respectively.

D. Mean flow and turbulence characteristics in downstream cross sections

The mean streamwise vorticity $\langle\omega_x\rangle$, velocity magnitude, and turbulence kinetic energy are plotted in various cross-sectional planes perpendicular to the streamwise (x) direction in Fig. 13.

In Fig. 13(a), pockets of large positive and negative $\langle\omega_x\rangle$ are shown, indicating that the secondary flow rotates in the counterclockwise and clockwise directions, respectively. At $x = 0$, such pockets are clearly visible near the bed and free surface at $y/L \approx 1.4$, which are the footprints of the horseshoe vortex and free-surface vortex systems, respectively. As the cross-sectional planes move downstream, those pockets gradually move away from the obstacle. Throughout the cross sections, in the vicinity of high $|\langle\omega_x\rangle|$, the velocity magnitude contours [Fig. 13(b)] appear distorted and high levels of k are observed [Fig. 13(c)], indicating the momentum redistribution and turbulence induced by the vortex system. In $2 \le x/L \le 7.5$, spiral streamline patterns appear at the location of those two vortex systems, clearly showing streamwise-oriented vortical structures. The absence of such distinct spiral streamline patterns between the sections $x/L = 0$ and 1 is because the trajectories of the horseshoe and free-surface vortex systems are not aligned with the main flow direction at those locations (see Fig. 12). Between $x/L = 2$ and 5, the horseshoe and free-surface vortex systems accompany additional vortex systems on the wake side, which rotate in opposite directions to their counterpart on the right side. As a result, four (or two pairs of) secondary current cells develop

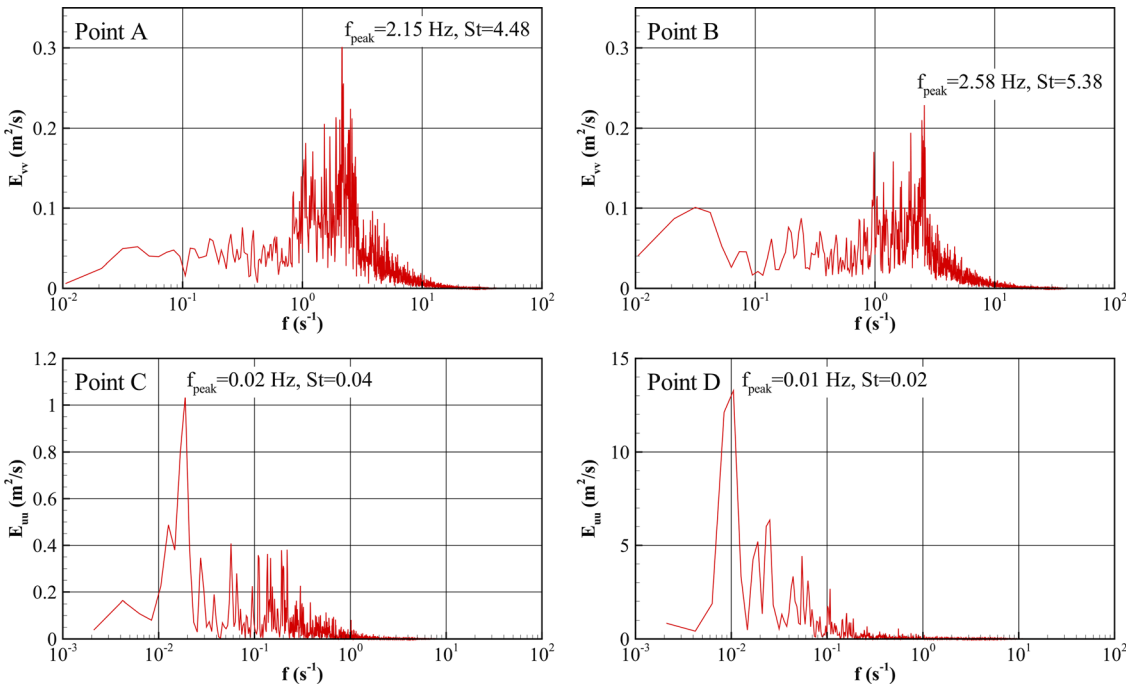

FIG. 10. Power spectral density of streamwise (E_{uu}) and transverse (E_{vv}) velocity fluctuations at Points A, B, C, and D. Their locations are shown in Figs. 7–9.

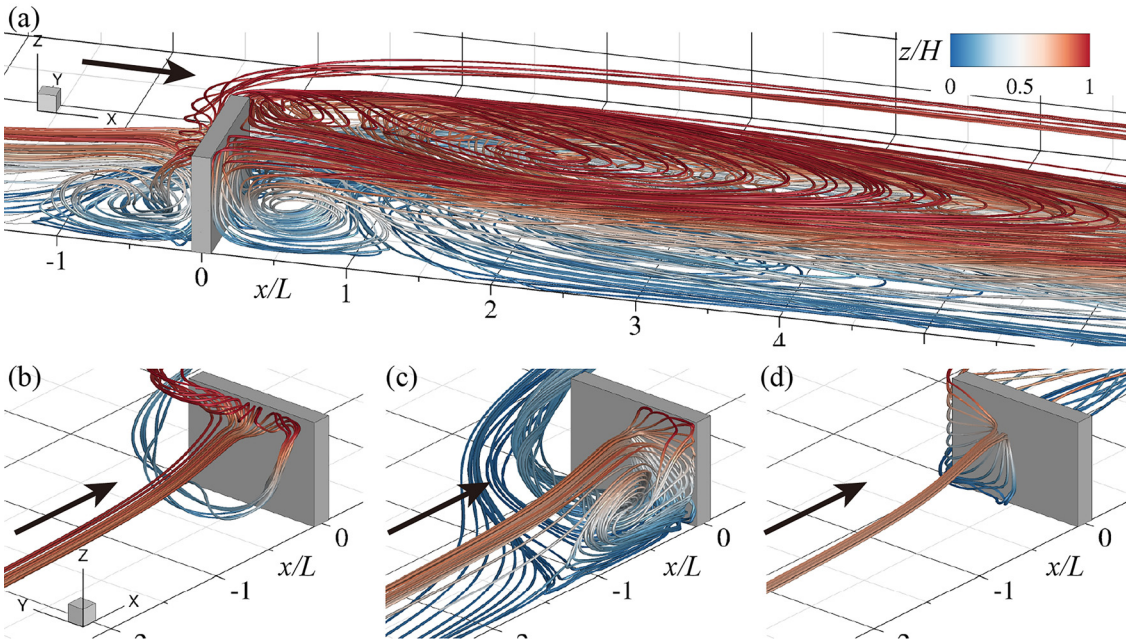

FIG. 11. Streamlines of the time-averaged flow colored by the dimensionless vertical coordinate (z/H). The arrows indicate the incoming flow direction. (a) Streamlines upstream and downstream of the obstacle; (b) streamlines near the free-surface; (c) streamlines passing the right half of the sidewall; (d) streamlines passing the left half of the upstream face.

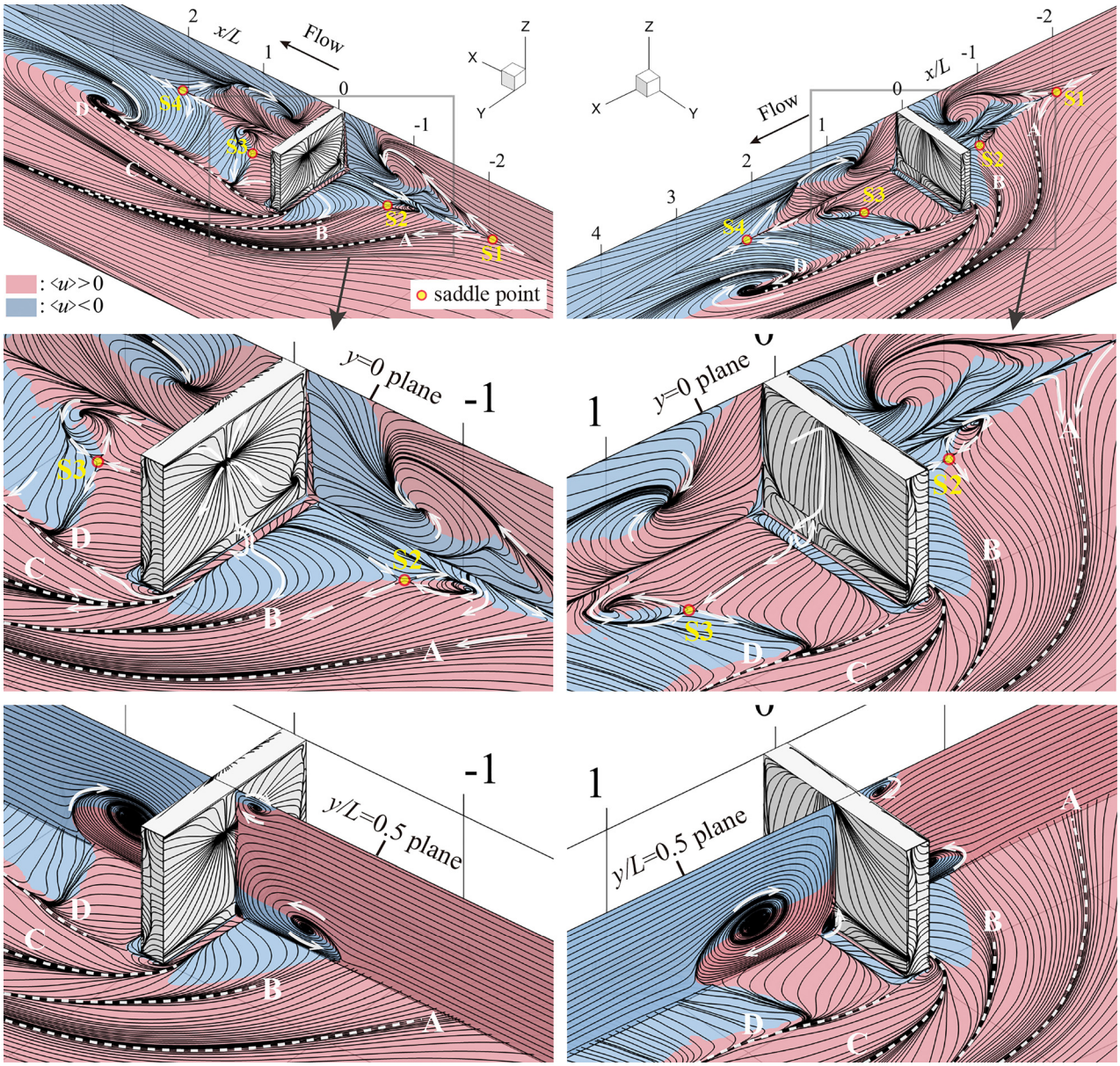

FIG. 12. Limiting streamlines of the time-averaged flow on the bed, the $y = 0$ sidewall, and obstacle surfaces.

downstream, which look approximately symmetric with respect to the mid-depth plane ($z/H = 0.5$). The fact that high levels of k are observed at the locations of the two wake-side secondary currents indicates that they are driven by turbulence.

Between the planes $x/L = 0$ and 0.5 in Fig. 13(c), a thin layer of very high k and mean velocity gradient is seen at locations slightly away from the obstacle edge ($y = L$). The layer features a two-dimensional (in the xy plane) shear layer generated by the vortex shedding from the upstream vertical edge of the obstacle. As the flow moves downstream, the shear layer becomes thicker in the spanwise direction. Compared to the mid-depth region, the thickness near the free surface and bed increases at a much faster rate particularly toward the wake. This phenomenon is associated with the two secondary currents on the wake side and features the shear layers penetrating into the wake. As shown in Fig. 13(b), this penetration results in the entrainment (momentum exchange) of the high-momentum incoming fluid into the wake near the bed and free surface.

The free-surface and horseshoe vortex systems, marked by the two circular pockets of high $|\langle\omega_x\rangle|$ and k outside the wake, gradually move away from the obstacle as the flow moves downstream. Owing

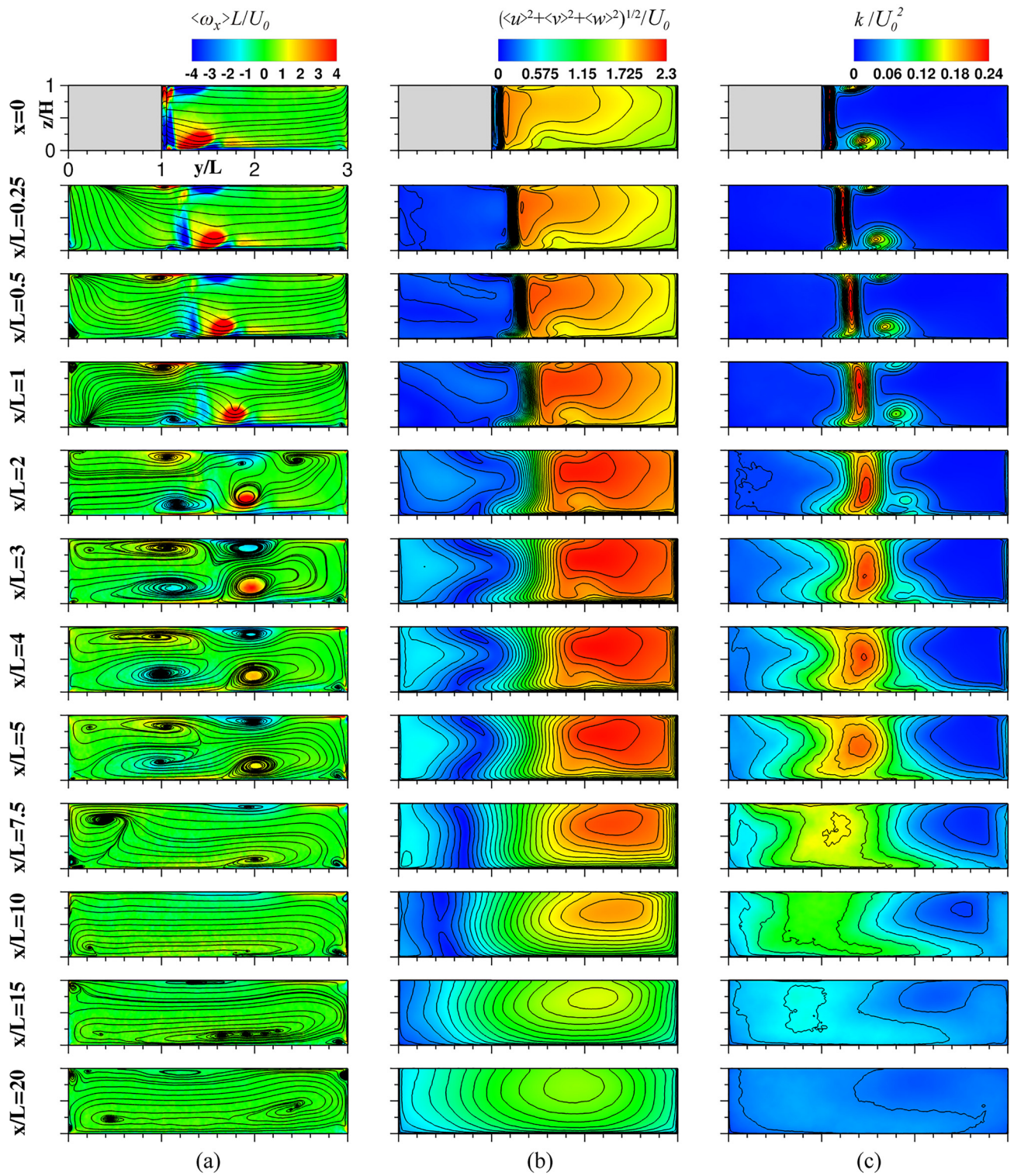

FIG. 13. The time-averaged flow quantities rendered dimensionless using U_0 and L at cross sections from $x/L = 0$ to 20. (a) Streamwise vorticity with superimposed streamlines, (b) velocity magnitude, and (c) turbulence kinetic energy. The plots are viewed from a location downstream of the sections. The contour line intervals in (b) and (c) are 0.1 and 0.02, respectively.

to the lateral spreading of the shear layer, the shear layer collides with the two vortex systems at $x \approx 1$. Following the collision, both vortices gradually breakdown, and they almost disappear at approximately $x/L = 7.5$.

E. Turbulence characteristics in horizontal planes

In Fig. 14, the contours of the computed second-order turbulence statistics, k, and the $\langle w'u' \rangle$ and $\langle u'v' \rangle$ Reynolds stresses are plotted in three xy planes at $z/H = 0.1$, 0.5, and 1 that are termed the lower-depth, mid-depth, and free-surface planes, respectively. For the lower-depth and mid-depth planes, the ADV measurements[10] are also plotted for comparison. As can be seen, the computation and measurement show excellent agreement.

The k contours in the three different planes commonly exhibit the lateral spreading of the shear layers in the spanwise direction that starts from the upstream corner of the obstacle. k is highest near the corner and gradually decreases in the downstream direction. The growth rate of the shear layer is fastest at the lower-depth plane and slowest at the mid-depth plane. The relatively faster growth rates in

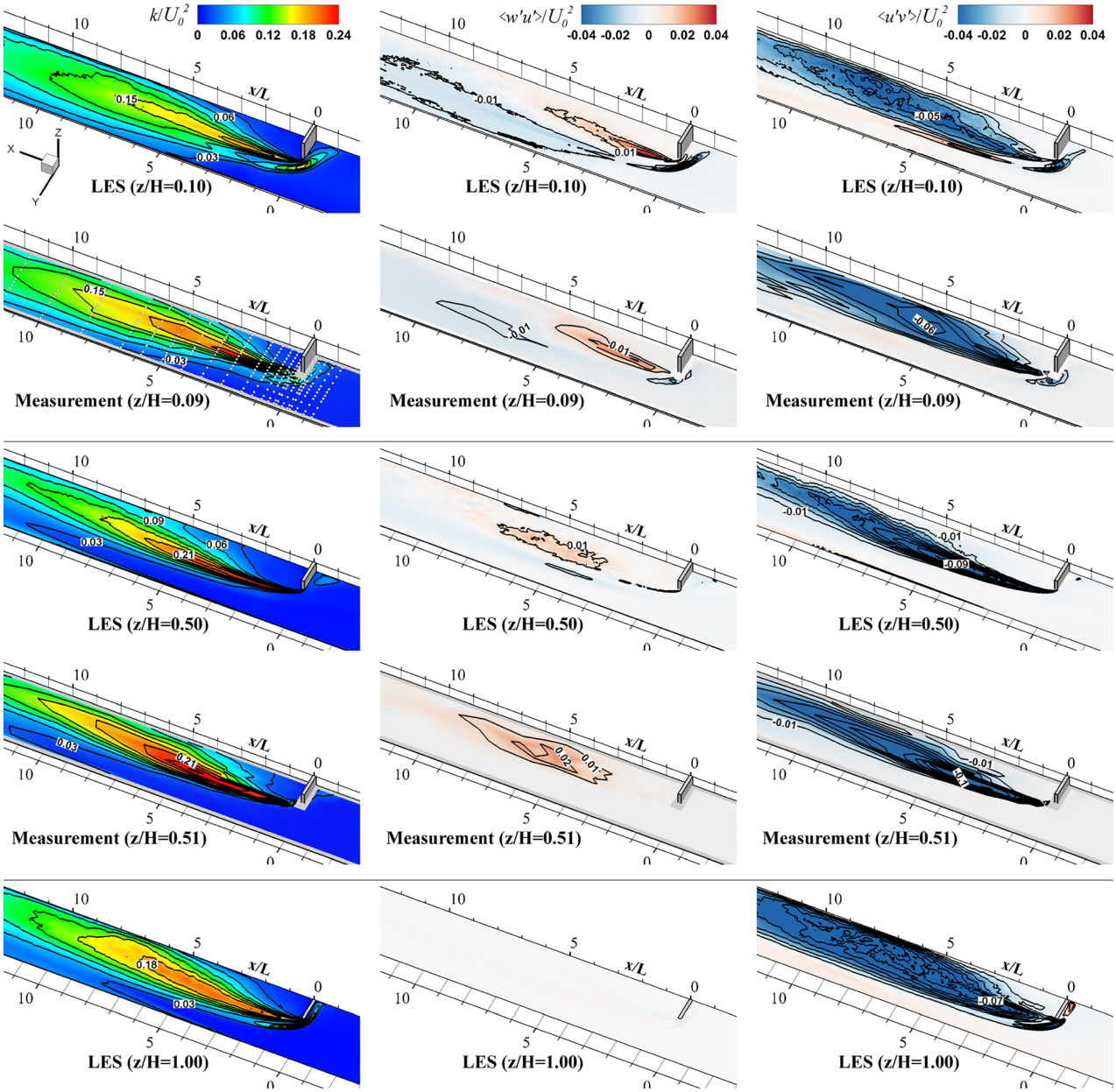

FIG. 14. Streamwise velocity and Reynolds shear stress contours in the xy planes at $z/H = 0.1$, $z/H = 0.5$, and $z/H = 1$.

the lower-depth and free-surface regions can be attributed to the increased turbulence intensity owing to the interaction of the shear layer with the horseshoe and free-surface vortex systems. The different shear layer growth rates across the depth may cause highly variable turbulence intensity within the same water column. For instance, it is clearly seen in $0.25 \leq x/L \leq 5$ of Fig. 13 that the k contours are highly distorted near the shear layers. Such non-homogeneous turbulence near the shear layer affects the overall turbulence anisotropy and spatial gradients of the Reynolds stresses that can create momentum redistribution through the terms for turbulent stress in the time-averaged Navier–Stokes equation.

The $\langle u'v' \rangle$ Reynolds stress implies the spanwise (y) shear of the streamwise velocity (u) and is associated with the turbulent mixing in the xy plane. In our case, this stress mostly induced by the shear layer emanating from the upstream edge of the obstacle. $\langle w'u' \rangle$ indicates the vertical (z) shear of the streamwise velocity ($\langle u \rangle$) and is associated with the turbulent mixing in the xz plane. In the present case, $\langle w'u' \rangle$ can be used as a measure of the three-dimensionality of the turbulence. As the figure shows, significant $\langle w'u' \rangle$ is found near the locations of the horseshoe vortex and secondary currents in the lower-depth and mid-depth planes. At the free surface, $\langle w'u' \rangle$ is almost negligible. It can be concluded that the wake shows predominantly two-dimensional turbulence characteristics near the free surface, but it shows three-dimensional characteristics around and below mid-depth.

F. Wall shear stress

Figure 15 shows contours of the dimensionless wall shear stress, τ/τ_0, where τ is the wall shear stress at a given location and $\tau_0 = \rho u_\tau^2$ is the mean bed shear stress of the incoming flow. Lines B, C, and D, shown in Fig. 12, are also displayed in this figure. The shear stress distribution reveals the following points.

First, the overall values of τ in the wake region are mostly below τ_0. In particular, a low τ is seen near the interface between the wake and shear layer and around the reattachment line on the sidewall. However, in some regions near and on the sidewall ($5 < x/L < 10$), τ exceeds τ_0. This is induced by a large negative $\langle u \rangle$ that develops near the sidewall within the horizontal recirculation zone. As seen in Fig. 13(b), the velocity magnitude in this region is up to 50% of the bulk inlet velocity. It is commonly believed that an obstacle placed near a channel bank can protect the bank erosion, but the present result indicates that a non-submerged obstacle may not provide such protection owing to the influence of the horizontal recirculation zone.

Second, the maximum τ occurs near the upstream corner of the obstacle, around which the horseshoe vortex passes. The maximum τ was approximately $17\tau_0$. This indicates that the horseshoe vortex is responsible for an increase in up to 17 times in the bed shear stress by compared with the mean value. Moreover, in the area between Lines B and C that lies underneath the horseshoe vortex system, a streak of high τ (5–$10\tau_0$) is observed. A high τ persists up to $x/L = 5$, where the horseshoe vortex system starts to lose its strength [Fig. 13(c)]. The above result suggests that under mobile bed conditions, local scour is expected to start at the upstream corner and propagate along the narrow area below the horseshoe vortex.

Third, τ is observed to be very low around the edge between the downstream face of the obstacle and bed, where the spanwise oriented recirculating flow region was observed [Fig. 11(a)]. This implies that although the streamline pattern of this region is somewhat similar to the horseshoe vortex, as discussed previously, the associated bed shear stress patterns and turbulence characteristics are significantly different.

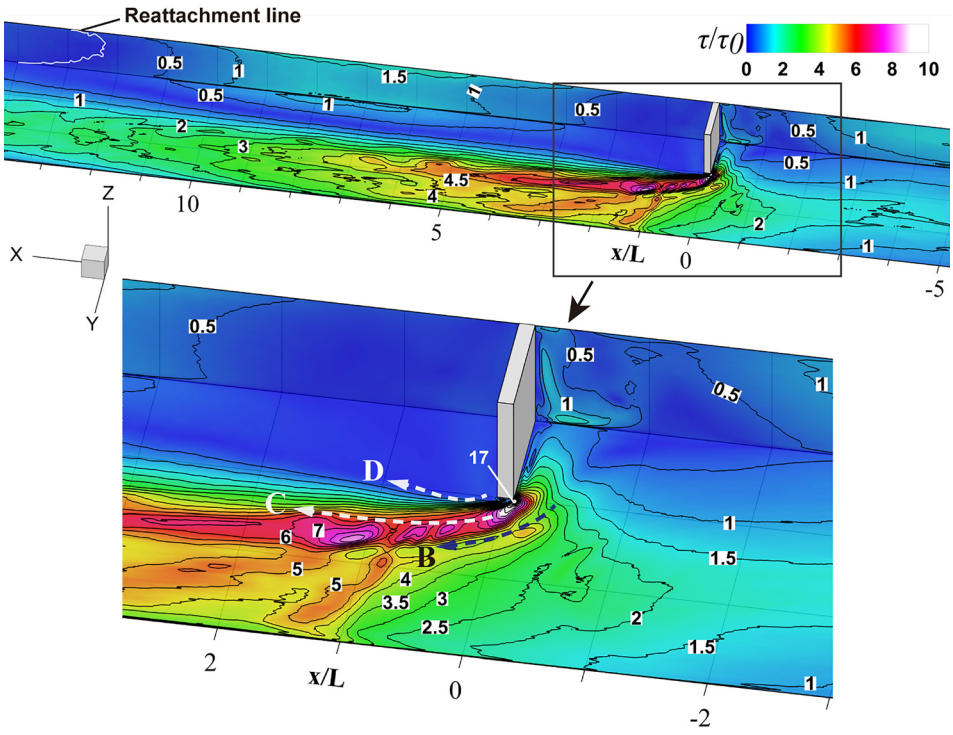

FIG. 15. Dimensionless wall shear stress contours at the bed and wake-side sidewall. The lines B, C, and D of the bottom figure are the same as those appear in Fig. 12. The contour intervals are spaced at $0.5\tau/\tau_0$.

As can be seen in Figs. 14 and 15, that region is associated with very low turbulence intensity and bed shear stress. Thus, one can expect sediment deposition in this region under mobile-bed conditions. This possibly explains the formation of a large deposition region behind a spur dike at $L/H = 1.5$ that was observed by Koken and Constantinescu.[19]

IV. SUMMARY AND CONCLUSIONS

In this study, the mean flow and turbulence characteristics around a non-submerged rectangular obstacle under a low L/H condition was investigated. The investigation involved an LES, performed at a resolution sufficiently fine to resolve near-wall regions and capture the instantaneous vortex shedding motions.

Our results show that the flow field in the vicinity of the obstacle is characterized by three different flow phenomena.

The first is the vortex shedding in an instantaneous sense and the shear layer in a time-averaged sense. This phenomenon occurs across the entire depth, and the flow structures are vertically oriented. The characteristic frequency of the shear layer motion near the obstacle is found to be $St \approx 4$–5. The second is the horseshoe vortex that originates from a sidewall upstream of the obstacle and moves parallel in front of the obstacle toward the channel center. The horseshoe vortex moves downstream forming an arch-shaped trajectory. This vortex is initially spanwise oriented upstream of the obstacle but becomes streamwise oriented while moving downstream. The third is the free-surface vortex, the structure of which is very similar to that of the horseshoe vortex, but with an opposite rotation. The vortex originates from the upper part of the upstream obstacle face and moves downstream, similar to the horseshoe vortex. The instantaneous flow fields at different time steps and the velocity spectra at locations near the bed and free surface reveal that both the free-surface and horseshoe vortex systems oscillate periodically in time in the streamwise direction upstream of the obstacle at a substantially lower frequency compared to the frequency observed in the far wake of the obstacle. The characteristic frequency associated with the free-surface and horseshoe vortex systems is found to be $St \approx 0.04$ and 0.02, respectively.

The present study also shows that the mean flow field in the cross-sectional planes of the wake is characterized by four secondary vortices. It was found that the formation of the vortices is induced by the interaction of the vertically oriented shear layer (from the obstacle tip), and the spanwise oriented horseshoe and free-surface vortices. The flow field in the horizontal plane of the wake, on the other hand, is characterized by a large horizontal recirculation zone spanning the entire wake and a smaller spanwise oriented recirculating flow region adjacent to the downstream face of the obstacle. Although the streamline patterns of the downstream spanwise oriented recirculating flow region look similar to those of the upstream horseshoe vortex, they show different turbulence characteristics. Whereas the horseshoe vortex is associated with high levels of turbulence and high bed shear stress, the other is associated with low levels of turbulence and low bed shear stress.

The wall shear stress distributions on the bed and sidewall provided useful information for understanding the sediment transport mechanism around the obstacle. The horseshoe vortex was found to significantly increase the bed shear stress in the region beneath its trajectory and around the upstream corner of the obstacle. Around the upstream corner, the maximum bed shear stress was approximately 17 times the mean bed shear stress of the incoming flow. Although the wall shear stress was observed to be mostly below the mean value in the wake region, in regions approximately $5L$ away from the obstacle, the wall shear stress was greater than the mean value probably due to the influence of the horizontal recirculation zone that induces a significant negative streamwise velocity near the sidewall. This result indicates that those regions are prone to erosion, which contradicts the conventional view that a bank-attached obstacle protects the bank. If a series of obstacles are employed, the high shear stress zone may be reduced or eliminated. This will require a separate study.

More studies will be necessary to fully understand the flow and turbulence mechanisms for bank-attached obstacles in an open channel, which have been widely used as a countermeasure to bank and bed erosion. There are a number of important research issues that need to be addressed in the future, including the investigation of wall shear stress fluctuations and bed morphodynamic changes in a channel, and the flow patterns and turbulence characteristics for an obstacle with higher L/H.

ACKNOWLEDGMENTS

This work was supported by the NRF (National Research Foundation) of Korea grant (No. NRF-2018R1D1A1B07049368).

DATA AVAILABILITY

The data of this study are available from the corresponding author upon reasonable request.

REFERENCES

[1]J. A. Gore and F. D. Shields, "Can large rivers be restored?," BioScience **45**, 142 (1995).
[2]B. Wu, G. Wang, J. Ma, and R. Zhang, "Case study: River training and its effects on fluvial processes in the Lower Yellow River, China," J. Hydraul. Eng. **131**, 85 (2005).
[3]C. Norberg, "Flow around rectangular cylinders: Pressure forces and wake frequencies," J. Wind Eng. Ind. Aerodyn. **49**, 187 (1993).
[4]S. Nakagawa, K. Nitta, and M. Senda, "An experimental study on unsteady turbulent near wake of a rectangular cylinder in channel flow," Exp. Fluids **27**, 284 (1999).
[5]D. Chen and G. H. Jirka, "The Japan society of fluid mechanics, find out more," Fluid Dyn. Res. **16**, 11 (1995).
[6]G. H. Jirka, "Large scale flow structures and mixing processes in shallow flows," J. Hydraul. Res. **39**, 567 (2001).
[7]S. Dey and A. K. Barbhuiya, "Flow field at a vertical-wall abutment," J. Hydraul. Eng. **131**, 1126 (2005).
[8]J. G. Duan, "Mean flow and turbulence around a laboratory spur dike," J. Hydraul. Eng. **135**, 803 (2009).
[9]M. Koken, "Coherent structures around isolated spur dikes at various approach flow angles," J. Hydraul. Res. **49**, 736 (2011).
[10]J. Jeon, J. Y. Lee, and S. Kang, "Experimental investigation of three-dimensional flow structure and turbulent flow mechanisms around a nonsubmerged spur dike with a low length-to-depth ratio," Water Resour. Res. **54**, 3530, https://doi.org/10.1029/2017WR021582 (2018).
[11]J. Higham, W. Brevis, C. Keylock, and A. Safarzadeh, "Using modal decompositions to explain the sudden expansion of the mixing layer in the wake of a groyne in a shallow flow," Adv. Water Resour. **107**, 451–459 (2017).
[12]J. Paik and F. Sotiropoulos, "Coherent structure dynamics upstream of a long rectangular block at the side of a large aspect ratio channel," Phys. Fluids **17**, 115104 (2005).
[13]S. Kang, A. Lightbody, C. Hill, and F. Sotiropoulos, "High-resolution numerical simulation of turbulence in natural waterways," Adv. Water Resour. **34**, 98 (2011).

[14]S. Kang and F. Sotiropoulos, "Assessing the predictive capabilities of isotropic, eddy viscosity Reynolds-averaged turbulence models in a natural-like meandering channel," Water Resour. Res. **48**, W06505, https://doi.org/10.1029/2011WR011375 (2012).
[15]S. Kara, M. C. Kara, T. Stoesser, and T. W. Sturm, "Free-surface versus rigid-lid les computations for bridge-abutment flow," J. Hydraul. Eng. **141**, 04015019 (2015).
[16]M. Koken and G. Constantinescu, "Flow and turbulence structure around a spur dike in a channel with a large scour hole," Water Resour. Res. **47**, W12511, https://doi.org/10.1029/2011WR010710 (2011).
[17]S. Kang, C. Hill, and F. Sotiropoulos, "On the turbulent flow structure around an instream structure with realistic geometry," Water Resour. Res. **52**, 7869, https://doi.org/10.1002/2016WR018688 (2016).
[18]Koken, M. and Constantinescu, G. "An investigation of the flow and scour mechanisms around isolated spur dikes in a shallow open channel: 1. Conditions corresponding to the initiation of the erosion and deposition process," Water Resour. Res. **44**, W08406, https://doi.org/10.1029/2007WR006489 (2008).
[19]M. Koken and G. Constantinescu, "An investigation of the flow and scour mechanisms around isolated spur dikes in a shallow open channel: 2. Conditions corresponding to the final stages of the erosion and deposition process," Water Resour. Res. **44**, W08407, https://doi.org/10.1029/2007WR006491 (2008).
[20]M. Koken and G. Constantinescu, "An investigation of the dynamics of coherent structures in a turbulent channel flow with a vertical sidewall obstruction," Phys. Fluids **21**, 085104 (2009).
[21]M. Germano, U. Piomelli, P. Moin, and W. H. Cabot, "A dynamic subgrid-scale Eddy viscosity model," Phys. Fluids A **3**, 1760 (1991).
[22]L. Ge and F. Sotiropoulos, "A numerical method for solving the 3D unsteady incompressible Navier–Stokes equations in curvilinear domains with complex immersed boundaries," J. Comput. Phys. **225**, 1782 (2007).
[23]S. Kang and F. Sotiropoulos, "Flow phenomena and mechanisms in a field-scale experimental meandering channel with a pool-riffle sequence: Insights gained via numerical simulation," J. Geophys. Res. **116**, F03011, https://doi.org/10.1029/2010JF001814 (2011).
[24]S. Kang and F. Sotiropoulos, "Numerical modeling of 3D turbulent free surface flow in natural waterways," Adv. Water Resour. **40**, 23 (2012).
[25]A. Khosronejad, T. Le, P. DeWall, N. Bartelt, S. Woldeamlak, X. Yang, and F. Sotiropoulos, "High-fidelity numerical modeling of the Upper Mississippi River under extreme flood condition," Adv. Water Resour. **98**, 97 (2016).
[26]T. B. Le, A. Khosronejad, F. Sotiropoulos, N. Bartelt, S. Woldeamlak, and P. Dewall, "Large-Eddy simulation of the Mississippi River under base-flow condition: Hydrodynamics of a natural diffluence-confluence region," J. Hydraul. Res. **57**, 836 (2019).
[27]S. Kang and F. Sotiropoulos, "Large-Eddy simulation of three-dimensional turbulent free surface flow past a complex stream restoration structure," J. Hydraul. Eng. **141**, 04015022 (2015).
[28]S. Kang and F. Sotiropoulos, "Numerical study of flow dynamics around a stream restoration structure in a meandering channel," J. Hydraul. Res. **53**, 178 (2015).
[29]S. Chawdhary, D. Angelidis, J. Colby, D. Corren, L. Shen, and F. Sotiropoulos, "Multiresolution large-Eddy simulation of an array of hydrokinetic turbines in a field-scale River: The Roosevelt Island Tidal Energy Project in New York City," Water Resour. Res. **54**, 10188, https://doi.org/10.1029/2018WR023345 (2018).
[30]S. Kang, A. Khosronejad, C. Hill, and F. Sotiropoulos, "Mean flow and turbulence characteristics around single-arm instream structures" J. Hydraul. Res. https://doi.org/10.1080/00221686.2020.1780494 (in press).
[31]S. Kang, A. Khosronejad, C. Hill, and F. Sotiropoulos, "Mean flow and turbulence characteristics around multiple-arm instream structures and comparison with single-arm structures," J. Hydraul. Eng. **146**, 04020030 (2020).
[32]S. Kang, I. Borazjani, J. A. Colby, and F. Sotiropoulos, "Numerical simulation of 3D flow past a real-life marine hydrokinetic turbine," Adv. Water Resour. **39**, 33 (2012).
[33]S. Kang, X. Yang, and F. Sotiropoulos, "On the onset of wake meandering for an axial flow turbine in a turbulent open channel flow" J. Fluid Mech. **744**, 376 (2014).
[34]X. Yang, S. Kang, and F. Sotiropoulos, "Computational study and modeling of turbine spacing effects in infinite aligned wind farms," Phys. Fluids **24**, 115107 (2012).
[35]S. J. Kim, J.-S. Jung, and S. Kang, "Fully three-dimensional Reynolds-averaged Navier–Stokes modeling for solving free surface flows around coastal drainage gates," J. Hydro-Environ. Res. **13**, 121 (2016).
[36]A. Khosronejad, S. Kang, and K. Flora, "Fully coupled free-surface flow and sediment transport modelling of flash floods in a desert stream in the Mojave Desert, California" Hydrol. Processes **33**, 2772 (2019).
[37]A. Khosronejad, S. Kang, I. Borazjani, and F. Sotiropoulos, "Curvilinear immersed boundary method for simulating coupled flow and bed morphodynamic interactions due to sediment transport phenomena," Adv. Water Resour. **34**, 829 (2011).
[38]A. Khosronejad, S. Kang, and F. Sotiropoulos, "Experimental and computational investigation of local scour around bridge piers," Adv. Water Resour. **37**, 73 (2012).
[39]A. Khosronejad, C. Hill, S. Kang, and F. Sotiropoulos, "Computational and experimental investigation of scour past laboratory models of stream restoration rock structures," Adv. Water Resour. **54**, 191 (2013).
[40]A. Khosronejad, S. Kang, A. Farhadzadeh, and F. Sotiropoulos, "On the genesis and evolution of barchan dunes: Hydrodynamics," Phys. Fluids **32**, 086602 (2020).
[41]S. Kang, A. Khosronejad, and F. Sotiropoulos, in *Environmental Fluid Mechanics*, Memorial Volume in Honour of Professor Gerhard H. Jirka (CRC Press, 2014), Chap. 7, pp. 123–151.
[42]M. A. Leschziner and W. Rodi, "Calculation of strongly curved open channel flow," J. Hydraul. Div. **105**, 1297 (1979).
[43]M. Wang and P. Moin, "Dynamic wall modeling for large-Eddy simulation of complex turbulent flows," Phys. Fluids **14**, 2043 (2002).
[44]S. Kang, "An improved near-wall modeling for large-Eddy simulation using immersed boundary methods," Int. J. Numer. Methods Fluids **78**, 76 (2015).
[45]J. Jeong and F. Hussain, "On the identification of a vortex," J. Fluid Mech. **285**, 69 (1995).
[46]H. Le, P. Moin, and J. Kim, "Direct numerical simulation of turbulent flow over a backward-facing step," J. Fluid Mech. **330**, 349 (1997).
[47]M. Tobak and D. J. Peake, "Topology of three-dimensional separated flows," Annu. Rev. Fluid Mech. **14**, 61 (1982).
[48]R. Martinuzzi and C. Tropea, "The flow around surface-mounted, prismatic obstacles placed in a fully developed channel flow (data bank contribution)," J. Fluids Eng. **115**, 85 (1993).
[49]W. J. Devenport and R. L. Simpson, "Time-dependent and time-averaged turbulence structure near the nose of a wing-body junction," J. Fluid Mech. **210**, 23 (1990).